ELSEVIER

Mechanics of Materials 18 (1994) 213–229

MECHANICS OF MATERIALS

Inelastic strains due to matrix cracking in unidirectional fiber-reinforced composites

M.Y. He [a], B.-X. Wu [a], A.G. Evans [a], J.W. Hutchinson [b,*]

[a] *Materials Department, College of Engineering, University of California, Santa Barbara, CA 93106-5050, USA*
[b] *Division of Applied Sciences, Harvard University, Cambridge, MA 02138, USA*

Received 1 November 1993; accepted 19 January 1994

Abstract

Simulations of the inelastic strains caused by matrix cracking in unidirectional CMCs are performed. They are based on a cell model, which has previously been analyzed by a shear lag approximation. Here, finite element solutions are used to arrive at more accurate formulae, differing from the shear lag results mainly in the range of small debonds. The model relates the inelastic strain to the constitutive properties, particularly the interface sliding and debonding resistances. Comparisons with experimental results indicate good correspondence for a SiC/SiC composite but divergences for a SiC/CAS composite. The divergences are attributed to the contribution of inelastic strain from fiber failure.

1. Introduction

In composites with either a ceramic (CMCs) or intermetallic (IMCs) matrix, cracks can form in the matrix while the fibers remain essentially intact (Aveston et al., 1971; Kim and Pagano, 1991; Marshall and Evans, 1985; Beyerle et al., 1992; Evans, 1991). This capability is imparted to the material by using a fiber coating that allows debonding and frictional sliding as the cracks interact with the fibers (Evans et al., 1991). Furthermore, in metal (MMCs) and polymer (PMCs) matrix materials, similar matrix cracks form upon cyclic loading. The matrix cracks may develop upon either tensile or shear loading (Brønsted et al., 1993). Both beneficial and detrimental effects arise when matrix cracks form. The *beneficial* effect occurs because the cracks introduce inelastic strains (Aveston et al., 1971; Nardonne and Prewo, 1988; Beyerle et al., 1992; Evans et al., 1993). Such strains provide stress redistribution mechanisms, which impart *notch insensitivity* when the composite constituents are *optimized* (Evans et al., 1993; Cady et al., 1993). For optimization purposes, it is important to understand the factors that govern the formation of matrix cracks, as well as their effect on the inelastic, or 'plastic', strains. The detrimental consequence concerns the *stress concentrations* induced in the fibers by matrix cracks, especially at ply interfaces and in the vicinity of manufacturing flaws (Budiansky and Cui, 1994). These stress concentrations, when they exist, may weaken the composite.

Most composites with practical utility include

* Corresponding author.

SSDI 0167-6636(94)00014-8

fibers having at least two orientations. The simplest such configuration is a 0°/90° laminated material such as that shown in Fig. 1. Analyses concerned with such materials are basic. Upon tensile loading, cracks in the 90° layers are first formed by a three dimensional tunneling process, spreading from initial flaws (Xia et al., 1993). At higher stresses, the cracks in the 90° plies begin to spread into neighboring 0° plies as plane strain matrix cracks, bridged by fibers. The associated uniaxial stress/strain behavior is depicted schematically in Fig. 2 (Beyerle et al., 1992; Evans et al., 1993). The behavior addressed in the present article concerns the tensile stress–strain behavior of 0° plies, following earlier work on the same problem (Pryce and Smith, 1992; Weitsman and Zhu, 1993; Evans et al., 1993; Vagaggini and Evans, 1993). The largest contributions to the inelastic strains arise due to matrix cracking and fiber debonding and sliding in the 0° plies. Knowledge of the behavior of these plies is an essential part of gaining an understanding of the performance of a laminated composite.

The inelastic strains caused by matrix cracks are most directly assessed on unidirectional materials. For such materials, the stress/strain behavior is sketched in Fig. 3. At stresses above $\bar{\sigma}_{mc}$, matrix cracks develop. The average spacing d between the matrix cracks diminishes as the stress increases. At $\bar{\sigma}_s$, the cracks saturate, with a spacing d_s. The slope of the stress/strain curve usually increases as the stress approaches and exceeds $\bar{\sigma}_s$. A methodology, described in references cited above, has been developed for predicting the uniaxial stress–strain behavior in terms of the constitutive properties of the fiber/matrix system such as fiber volume fraction, interface debond energy, frictional sliding stress, and residual stresses. For the most part, solutions available for carrying out this methodology are obtained from approximate shear lag analyses. The primary purpose of this paper will be to present a fairly comprehensive set of more accurate results which will allow assessment of the shear lag predictions

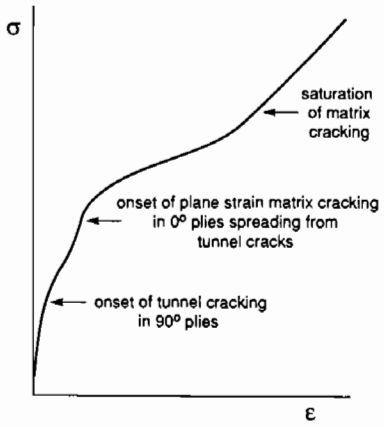

Fig. 2. Schematic tensile stress–strain curve of a cross-ply composite.

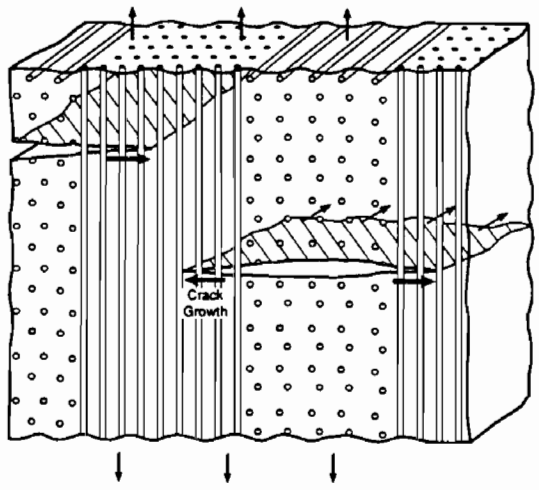

Fig. 1. A cross-ply composite with tunnel cracks, which have first formed in the 90° plies, spreading as plane strain cracks into the 0° plies.

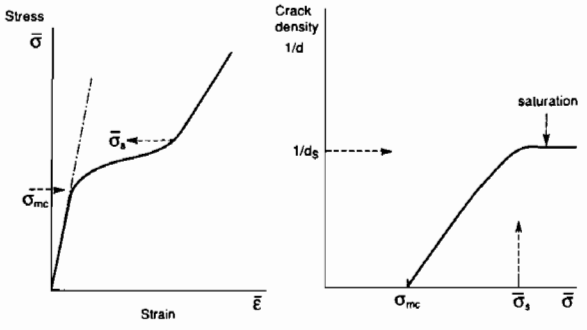

Fig. 3. Tensile stress–strain behavior of a uni-directional fiber reinforced composite stresses parallel to the fibers, and evolution of matrix crack density.

and, more importantly, to enable workers in the field to carry out accurate implementation of the general methodology.

2. Preliminaries and results from shear lag analysis

The focus will be on the stress–strain behavior of a unidirectional fiber reinforced composite under uniaxial stressing parallel to the fibers such that the overall strain is monotonically increasing. Fig. 3 depicts the stress–strain behavior of such a composite. As already remarked, matrix cracks begin forming when the overall stress $\bar{\sigma}$ reaches the matrix cracking stress $\bar{\sigma}_{mc}$ with debonding and sliding occurring along the fiber/matrix interfaces. Let E be the modulus of the uncracked composite. There are several contributions to the overall strain $\bar{\epsilon}$ in addition to the strain expected for the uncracked composite, $\bar{\sigma}/E$. Even without debonding and sliding, the matrix cracks increase the compliance of the composite. Debonding and sliding further increase the compliance and thereby add to the overall strain. The modulus of the cracked and debonded composite at a *fixed average spacing* of matrix cracks d and at a *fixed* debond length l (see Fig. 4) will be denoted as E_c such that in the absence of interface friction and of any residual stress

$$\bar{\epsilon} = \bar{\sigma}/E_c. \tag{1}$$

Friction along the fiber/matrix interface reduces the overall strain relative to (1). Conversely, a residual tensile stress in the matrix is relieved by matrix cracking and gives rise to additional overall straining relative to (1).

In this paper, attention is restricted to systems with a residual compressive stress acting across the fiber/matrix interface such that the debonding process involves mode II cracking and such that the debonded interfaces remain closed. A constant friction stress τ is assumed to act within the debond region as depicted in Fig. 4. The misfit strain giving rise to residual stress in the uncracked composite is denoted by Ω. Following the scheme in Hutchinson and Jensen (1990, hereafter designated by HJ), Ω is identified with

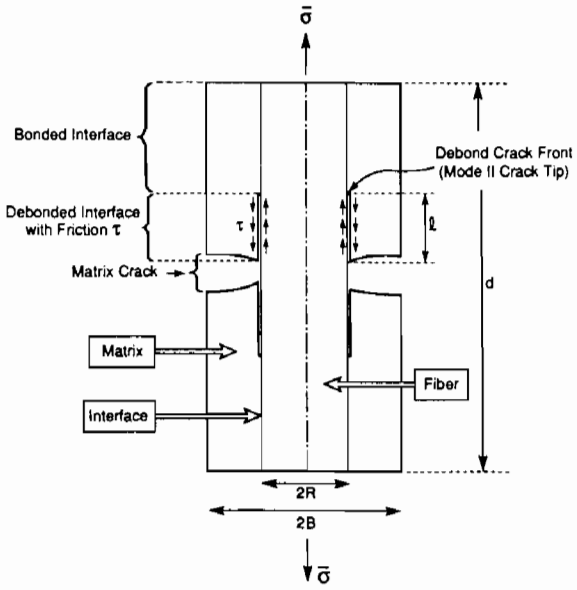

Fig. 4. Conventions for axisymmetric cell model.

the axial strain mismatch between the fiber and the matrix such that a positive Ω corresponds to residual tension in the matrix. A difference in radial and axial strain mismatches between the fiber and matrix is taken into account; $\lambda\Omega$ denotes the radial strain mismatch. The results for the quantities of interest will be calculated using the axisymmetric cell displayed in Fig. 4. Details of the specification of this cell will be given in the next section, as will the method for calculating the quantities which follow. In the remainder of this section, we present the form of the mechanics solution for this cell model, introducing the essential nondimensional coefficients. We also present the approximate results from shear lag analysis for these coefficients. In the next section, the more accurate results for the coefficients based on full numerical calculations will be given along with some further motivation for the particular form of the mechanics solutions, as well as assessments of the shear lag approximations.

2.1. Form of the mechanics solution

At *fixed* average matrix crack spacing d and at *fixed* debond length l, the overall strain depends

linearly on $\bar{\sigma}$, τ and Ω. Specifically, for the cell model of Fig. 4 the solution for the overall strain can be written as

$$\bar{\epsilon} = \frac{\bar{\sigma}}{E_c} + D_1 \frac{\Omega E_m f a_2 R}{E(1 - a_1 f) d} - D_3 \frac{\tau l^2}{ERd}, \tag{2}$$

where the incremental modulus of the cracked and debonded composite is written as

$$\frac{1}{E_c} = \frac{1}{E}\left(1 + \frac{D_1 R}{d}\right). \tag{3}$$

In these equations R is the radius of the fiber, $f = (R/B)^2$ is the volume fraction of fibers where B is the outer radius of the cell, and E_m is the matrix modulus. The coefficients a_i, (and b_i and c_i introduced in subsequent equations) are coefficients introduced in HJ. Recipes for these coefficients are given in HJ for arbitrary fiber and matrix moduli, including the most general cases where the fiber has transversely isotropic moduli, the matrix is isotropic, and the ratio of the radial to axial mismatch strains is λ. Except when indicated to the contrary, the appropriate coefficients for the present work are those in HJ associated with type II boundary conditions (see the discussion in the next section). The coefficients D_i in (2) and (3), and in (4) given further, are nondimensional functions of f, l/R, d/R and nondimensional moduli parameters, such as E_f/E_m, ν_f and ν_m. These are the coefficients for which extensive numerical results will be presented in the next section. We note in advance that their dependence on d/R is relatively weak over most of the parameter range of interest and for many purposes this dependence can be neglected. For *fixed* d and l the mode II stress intensity factor K_{II} is also a linear function of $\bar{\sigma}$, τ and Ω. The form of the solution for K_{II} for the cylindrical cell of Fig. 4 is

$$K_{II} = D_2 \bar{\sigma}\sqrt{R} + D_2 \frac{\Omega E_m f a_2 \sqrt{R}}{(1 - a_1 f)} - D_4 \frac{\tau l}{\sqrt{R}}. \tag{4}$$

The fact that D_1 appears in the contributions in (2) from both $\bar{\sigma}$ and Ω, and D_2 in the corresponding contributions in (4), is a rigorous feature of the solution which is shown in the next section.

The energy release rate G of the mode II debond crack is related to K_{II} by

$$G = K_{II}^2 / \hat{E}, \tag{5}$$

where $\hat{E}$ is a modulus quantity dependent on the moduli of the fiber and the matrix. When the fiber and matrix are each isotropic,

$$\frac{1}{\hat{E}} = \tfrac{1}{2}(1 - \beta^2)\left(\frac{1 - \nu_f^2}{E_f} + \frac{1 - \nu_m^2}{E_m}\right), \tag{6}$$

where β is the second plane strain Dundurs parameter. For most systems the numerical influence of β^2 in (6) is quite small and can be neglected.

2.2. Shear lag results for D_i

Shear lag modeling of fiber debonding and frictional sliding for systems where the fiber/matrix interface remains closed, have been carried out by a number of authors (Gao et al., 1988; Marshall, 1992; HJ). Here the results of HJ will be used and these can be expressed in the form given in (2) and (4). (Indeed, it was the form of the shear lag results which, in part, guided the choice of these forms.) The expressions for D_i listed in (7a)–(7d) are obtained by identification from the HJ expressions. Specifically,

$$D_1 = 8f \frac{E}{E_m} \frac{l}{R} c_1^2, \tag{7a}$$

$$D_2 = \sqrt{\hat{E}/E_m}\, c_1, \tag{7b}$$

$$D_3 = 2 \frac{E}{E_m} b_2, \tag{7c}$$

$$D_4 = \sqrt{(b_2 + b_3)\left(\hat{E}/E_m\right)}. \tag{7d}$$

The relevant recipes for the coefficients above are those for the type II boundary conditions in HJ, which are appropriate to the present study because they model a cell in an array as discussed in the following. It should be remarked that the

above result for D_2 is not from a shear lag calculation. Instead, it is the exact result for the cylindrical model of Fig. 4 for the case $d/R = \infty$ in the steady-state limit when l/R becomes sufficiently large. Nevertheless, for brevity, the above set of formulas will be referred to collectively as the shear lag approximation.

3. Numerical results for D_i

3.1. The cell model

The scheme behind the model envisages a hexagonal array of fibers in a matrix with uniformly spaced matrix cracks aligned normal to the fiber direction. As is now common practice, for computational reasons, a cylindrical cell is used to approximate the hexagonal cell (cf. Fig. 5 and Fig. 4). The cell is subject to an overall stress, $\bar{\sigma}$, parallel to the fiber axis, and the height of the cell is taken to be equal to the crack spacing, d. The cell has a matrix crack at its mid-plane. The lateral faces are required to remain a circular cylinder with zero shear traction and zero average normal traction. The faces of the cell perpendicular to the stressing direction are constrained to remain planar with zero shear traction and with *average* normal traction equal to $\bar{\sigma}$. As already introduced, the volume fraction of the fiber is $f = (R/B)^2$, where B is the cell radius; l is the length of the debond zone. Residual compressive stress is assumed to act across the fiber matrix interface keeping the debonded interface closed.

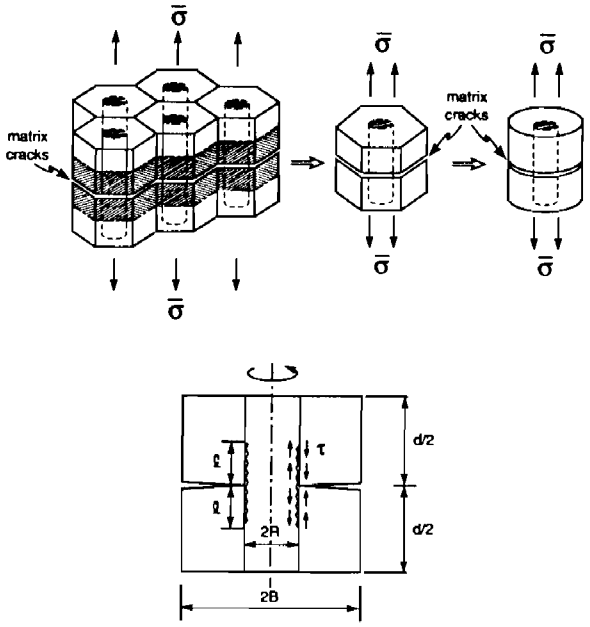

Fig. 5. Motivation for axisymmetric cell model.

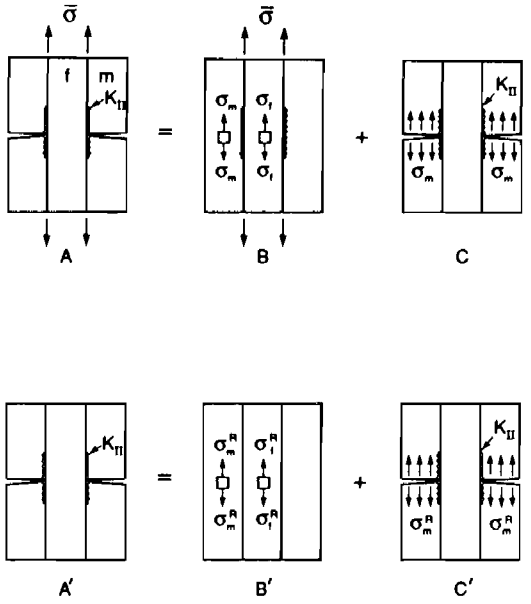

Fig. 6. Solution schematics for establishing the connection between solutions for two loadings.

The appearance of D_1 in the two contributions in (2) and D_2 in the two terms in (4) is a rigorous consequence of the close connection of the effects of applied stress and residual stress on the overall strain and the stress intensity factor due to cracking and debonding. The connections are now established with the aid of the solution schematics in Fig. 6. Prior to any cracking or debonding, the two contributions to the axial stress in the fiber and the matrix are given by results from the appropriate Lame problem in HJ:

$$\sigma_f = a_1 \bar{\sigma}$$

and

$$\sigma_f^R = -a_2 E_m \Omega, \tag{8a}$$

$$\sigma_m = (1 - a_1 f)\bar{\sigma}/(1-f)$$

and

$$\sigma_m^R = f a_2 E_m \Omega/(1-f). \tag{8b}$$

The additional overall strain due to cracking and debonding (with zero friction) in the presence of $\bar{\sigma}$ is given by problem C in Fig. 6; denote it by $\Delta\bar{\epsilon} = (\sigma_m/E_m)h$, where h is a dimensionless function of the geometric and moduli variables. By (2) and (3), h and D_1 are connected by

$$h = D_1 \frac{(1-f)E_m R}{(1-a_1 f)Ed}. \tag{9}$$

Now consider the additional overall strain due to release of the residual stress. From problem C′ in Fig. 6, this is $\Delta\bar{\epsilon} = (\sigma_m^R/E_m)h$, where h is the same as in problem C. The expression in (2) for the contribution due to Ω immediately follows using (11b) and (12). The argument for the dual roles of D_2 in (4) is similar.

3.2. Numerical results and more accurate formulas for D_i

Plots of D_1 as a function of l/R are shown in Fig. 7a for three levels of fiber volume fraction and three values of E_f/E_m; $d/R = 16$ has been chosen for this cell. The results in this plot, and others to follow for the cell model, have been computed with $\nu_f = \nu_m = 0.3$. The value of D_1 for $l = 0$, D_1^0, reflects the compliance increase due to matrix cracks without debonding. Plots of D_1^0 computed, again with $d/R = 16$, are given in Fig. 7b. When used in (3), the results for D_1^0 in Fig. 7b provide an estimate of compliance which is valid for sufficiently dilute crack spacings, typically d greater than about one fiber diameter. Estimates of D_1^0 which account for crack interaction could be presented but are generally not needed for the present purposes since the crack spacing only drops to values as small as several fiber diameters when appreciable debonding occurs as well. Under these circumstances the predominant contribution arises from the fiber/matrix sliding, as can be seen in Fig. 7a. The linear dependence of D_1 on l evident in Fig. 7a persists until the debond is within about one radius of the cell end. As the debond reaches the end of the cell (i.e. $l = d/2$) the value of D_1 then drops to the HJ result (7a). An approximation which captures the various features mentioned above is

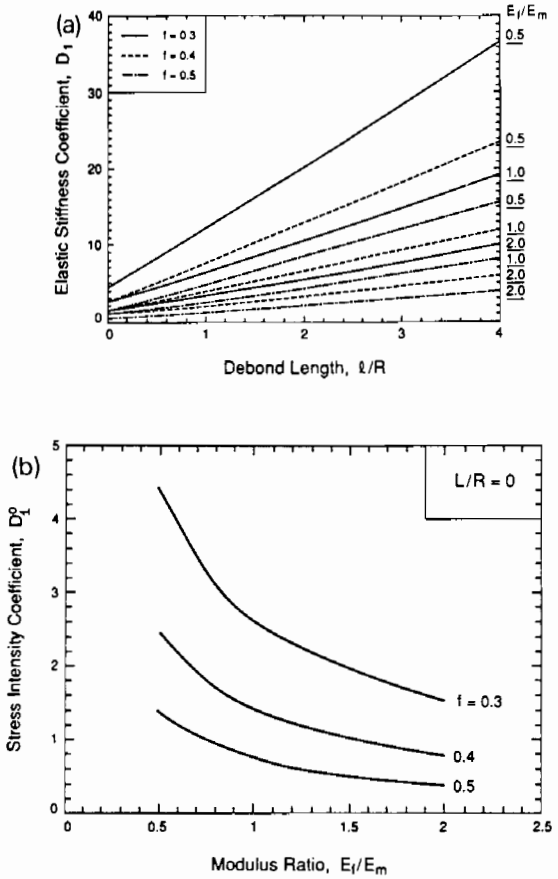

Fig. 7. Numerical results from cell model: (a) for D_1; (b) for values of D_1 in absence of any debonding of D_1^0.

$$D_1 = D_1^0\left(1 - \frac{2l}{d}\right) + 8f\frac{E}{E_m}\frac{l}{R}c_1^2. \tag{10}$$

Numerical results for D_2 for the same sets of parameters are shown as a function of l/R in Fig. 8. The results from (7b) from the steady-state limit are included. The slow, slight increase of the

numerical results above the steady-state limit as l/R increases above about 3 or 4 is due to the interaction between l and d, i.e. and influence of d/R. But this influence is quite small until the debond approaches the end of the cell. The results presented here were computed for a cell with $d/R = 16$. The steady-state estimate of D_2 is also in error as l/R becomes less than about $1/2$, but that too can probably be overlooked in most applications of the present results since the details of the emerging debond precipitated by the matrix crack are likely to be fairly complicated and three dimensional in nature. In conclusion, the steady-state estimate (7b) of D_2 should be sufficiently accurate for use in (4).

The reduction in the overall strain caused by the friction between the fiber and the matrix is given by the third term in (2). Numerical results for D_3 are plotted in Figs. 9a and 9b. Since the dependence of D_3 on l/R is very strong as l/R becomes small, the abscissa in Fig. 9a is taken to be the inverse normalized debond length. As l/R becomes large, the numerical results for D_3 do approach the shear-lag prediction (7c), but clearly there are significant discrepancies at smaller l/R. An approximation for D_3 is developed in the Appendix. It has the features that it approaches the shear-lag result (7c) as l/R becomes large

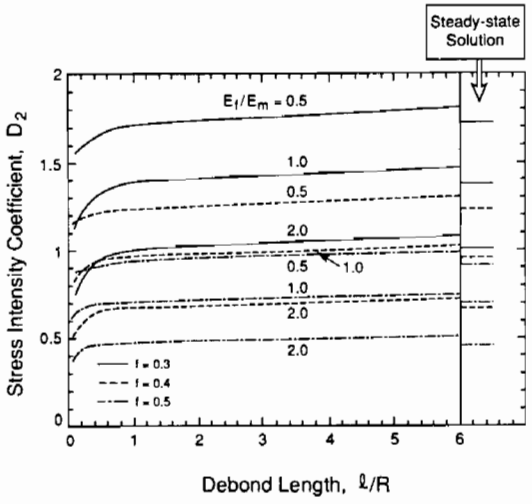

Fig. 8. Numerical values for D_2 from cell model.

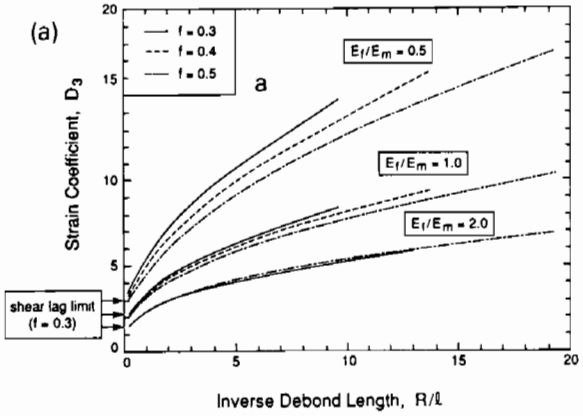

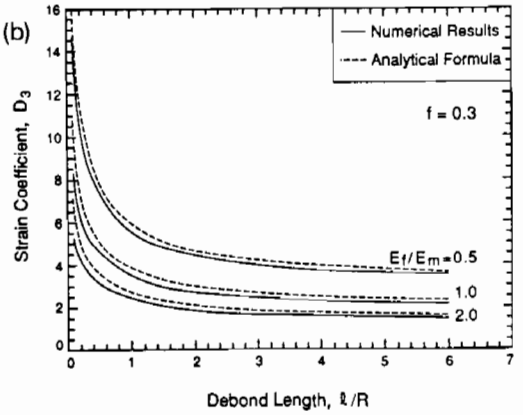

Fig. 9. Numerical values from cell model: (a) for D_3 as a function of inverse debond length; (b) compared with formula (11).

and approaches an approximation to the asymptotic solution when l/R is small; it is

$$D_3 = \left\{ \left[\left(\frac{32}{3} \sqrt{\frac{2}{\pi}} \right) \frac{fc_1 E}{\sqrt{\hat{E} E_m}} \sqrt{\frac{R}{l}} \right]^2 + \left(2 \frac{E}{E_m} b_2 \right)^2 \right\}^{1/2} . \tag{11}$$

Comparisons of the prediction from (11) with some of the numerical results for $f = 0.3$ are shown in Fig. 9b where it is seen that the approximate formula (11) gives a reasonably accurate interpolation over the entire range of l/R.

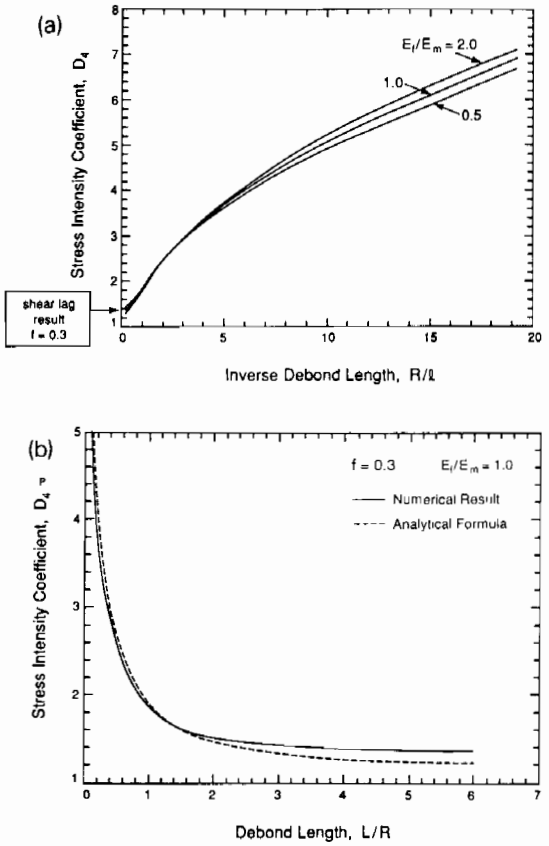

Fig. 10. Numerical values from cell model: (a) for D_4 as a function of inverse debond length; (b) compared with formula (12).

The frictional reduction in the mode II stress intensity factor depends on D_4, as plotted in Figs. 10a and 10b. This coefficient has a very strong dependence on l/R but almost no dependence on f. The approach to the shear lag result as l/R increases is very slow. The strong dependence on l/R is again addressed by an interpolation approximation obtained in the Appendix, which approaches the shear lag result (7d) for large l/R and approaches an approximation to the asymptotic solution for the limit of small l/R. This interpolation formula is

$$D_4 = \left\{ \left(\frac{\pi R}{l} \right)^2 + \left[(b_2 + b_3) \left(\frac{\hat{E}}{E_m} \right) \right]^2 \right\}^{1/4} . \qquad (12)$$

A comparison between (12) and the more accurate numerical results in Fig. 10b shows that (12) provides an adequate approximation to D_4 over the entire range of l/R, although not quite as accurate as the approximation for D_3.

4. Prediction of tensile stress–strain behavior

4.1. Behavior prior to matrix crack saturation

Debonding is controlled by the mode II debonding toughness Γ_i. The matrix crack spacing $d(\bar{\sigma})$ is a function of the applied stress. This functional dependence is assumed to be known from experimental observation or from other theoretical modeling (Curtin, 1993; Spearing and Zok, 1993); no attempt is made to predict $d(\bar{\sigma})$ here. The relationship between the debond length l and the applied stress $\bar{\sigma}$ is obtained from (4) by imposing the debond condition $K_{II} = \sqrt{\hat{E}\Gamma_i}$. Let $\bar{\sigma}_i$ be the debond initiation stress, defined as the overall stress at which the debond can begin to spread up the fiber from the matrix crack surface. This stress can be larger or smaller than the matrix cracking stress, depending on the properties of the composite. If it is larger, debonding is postponed beyond the onset of matrix cracking until the overall stress reaches $\bar{\sigma}_i$; if it is smaller, the debond jumps to a finite length as soon as a matrix crack forms. From (4) and (7b), the debond initiation stress is

$$\begin{aligned} \bar{\sigma}_i &= (1/D_2)\sqrt{\hat{E}\Gamma_i/R} - fa_2 E_m \Omega/(1 - fa_1) \\ &= (1/c_1)\sqrt{E_m \Gamma_i/R} - (c_2/c_1) E_m \Omega \qquad (13) \\ &\equiv \bar{\sigma}_D - \bar{\sigma}_R . \end{aligned}$$

Since D_2 is given by (7b) for the more accurate results as well as for the shear lag model, this result holds for both levels of approximation. Eq. (7b) has been used to arrive at the second expression, along with the identity $c_2/c_1 = fa_2/(1 - fa_1)$ from HJ. The third line in (13) is used to define the two contributions to $\bar{\sigma}_i$, one due to the mode II debond toughness and the other due to the

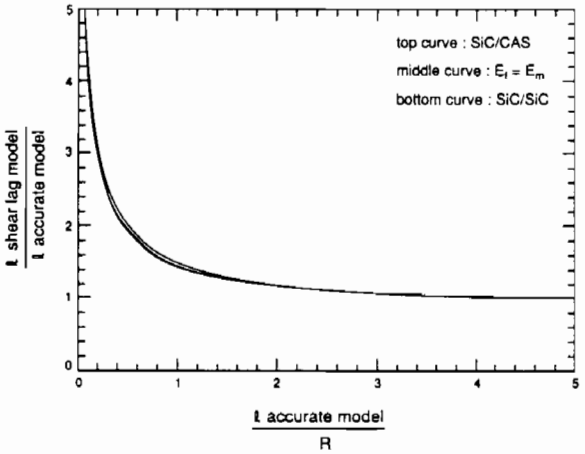

Fig. 11. Ratio of debond length predicted by shear lag model to that predicted by cell model as a function of normalized debond length from cell model.

residual stress in the uncracked composite. For applied stresses greater than $\bar{\sigma}_i$, (4) gives

$$\frac{l}{R} = \frac{D_2}{D_4(l)} \frac{(\bar{\sigma} - \bar{\sigma}_i)}{\tau}. \tag{14}$$

One of the main differences between predictions from the more accurate cell model and the shear lag model is the debond length when it is not large. By (14) with (7d) and (12), the ratio of the predicted debond lengths at a given value of applied stress depends on l/R from the more accurate model according to

$$\frac{l_{\text{shear lag model}}}{l_{\text{accurate model}}} = \left\{1 + \left(\frac{\pi R}{l}\right)^2 \left[(b_2 + b_3)\left(\frac{\hat{E}}{E_m}\right)\right]^{-2}\right\}^{1/4}. \tag{15}$$

Plots of this ratio are presented in Fig. 11. It can be seen that there is little dependence on the moduli choices, but the shear lag model significantly overestimates the extent of debonding for debonds less than about one fiber diameter.

The relation (14) giving l/R, together with $d(\bar{\sigma})$, can now be used in conjunction with (2) to predict $\bar{\epsilon}$ as a function of $\bar{\sigma}$. The l-dependence of D_1 and D_3 in (2) and of D_4 in (14) must be taken into account. The most straight-forward procedure to generate stress–strain curves with these relations is to use l as a free parameter which is increased monotonically (until it reaches $d/2$), using (14) to obtain $\bar{\sigma}$ and then (2) to obtain $\bar{\epsilon}$. Specific examples will be given in Section 5 where they will be compared with closed form representations for the stress–strain behavior valid for a shear lag approximation given in Section 4.3.

4.2. Consistency condition for the cell height d_s at matrix crack saturation

With reference to Fig. 3, let $\bar{\sigma}_s$ be the overall stress at which the matrix cracking saturates at spacing d_s. In modeling the response of the composite by a representative cell of height d, we do not attempt to capture the statistics of the matrix cracking process wherein new cracks form at randomly located flaw sites in portions of the composite which have not yet experienced fiber debonding and sliding. Here we will assume that the matrix cracks are uniformly spaced with the spacing d identified as the cell height. For this model, d decreases and l increases as $\bar{\sigma}$ is increased. Additional matrix cracks cannot be nucleated once complete fiber debonding has occurred. Conversely, further matrix cracks will nucleate under increasing stress if the fibers have not fully debonded. It follows, then, that within the framework of this model, $\bar{\sigma}$ must attain $\bar{\sigma}_s$ as the fibers become fully debonded (i.e., as l approaches $d/2$). By (14), this requirement provides the consistency relation between d_s and $\bar{\sigma}_s$ as

$$\frac{d_s}{R} = \frac{2D_2}{D_4(d_s/2)} \frac{(\bar{\sigma}_s - \bar{\sigma}_i)}{\tau}. \tag{16}$$

Well-known statistical arguments (e.g. Curtin, 1993) suggest that the mean matrix crack spacing at saturation should fall between d_s as predicted by (16) and $d_s/2$. A limitation of any model based on a single representative cell is that it cannot realistically reproduce the effects of variations in the matrix crack spacing. Here, (16) will be used to specify the limit when matrix crack saturation occurs, denoting also the point where the fibers have fully debonded.

4.3. Specialization to the shear lag approximation

The above prescriptions simplify for the shear lag approximations of D_i in Section 2.2. Now, D_4 is independent of l in (14). In evaluating $\bar{\epsilon}$ using (2) for $\bar{\sigma} < \bar{\sigma}_s$, D_3 is independent of l and D_1 varies linearly with l. By eliminating l in (2) using (14), one can readily obtain an equation of the form

$$\bar{\epsilon} = \frac{\bar{\sigma}}{E} + \frac{1}{d(\bar{\sigma})}\left[A_1(\bar{\sigma}-\bar{\sigma}_i)^2 + A_2(\bar{\sigma}-\bar{\sigma}_i)\right], \tag{17}$$

where the coefficients A_1 and A_2 involve the HJ coefficients and parameters such as τ and Γ_i.

A further simplification is achieved if one assumes that $\nu_f = \nu_m = \nu$ and if one uses the formulas in HJ for type I boundary conditions rather than type II conditions. Type I conditions are appropriate for a cell with completely unconstrained lateral sides; these are the conditions assumed by most authors in carrying out shear lag analyses. Some discussion is given in the Appendix concerning the error involved in making this replacement , which is generally small for the present purposes. Under these conditions, (14) and (17) reduce exactly to, respectively,

$$\frac{l}{R} = \frac{(1-f)}{2f}\frac{E_m}{E}\frac{(\bar{\sigma}-\bar{\sigma}_i)}{\tau}, \tag{18a}$$

$$\bar{\epsilon} = \frac{\bar{\sigma}}{E} + \frac{1}{d(\bar{\sigma})}\left(\frac{(1-f)^2E_m^2R}{2f^2E^2E_f\tau\chi^2}\right) \times\left[(\bar{\sigma}-\bar{\sigma}_i)^2 + 2\bar{\sigma}_D(\bar{\sigma}-\bar{\sigma}_i)\right], \tag{18b}$$

$$\bar{\sigma}_i = \bar{\sigma}_D - \bar{\sigma}_R,$$

$$\bar{\sigma}_D = \chi\sqrt{\frac{4f^2E_fE\Gamma_i}{(1-f)E_mR}},$$

$$\bar{\sigma}_R = \frac{E}{E_m}\sigma_m^R, \tag{18c}$$

where χ is a factor close to unity given by

$$\chi = \sqrt{\frac{(1+\nu)E_f + (1-\nu)E}{(1+\nu)[E_f + (1-2\nu)E]}}. \tag{18d}$$

The consistency condition (16) becomes

$$\frac{d_s}{R} = \frac{(1-f)}{f}\frac{E_m}{E}\frac{(\bar{\sigma}_s-\bar{\sigma}_i)}{\tau}. \tag{19}$$

4.4. Stress–strain behavior subsequent to matrix crack saturation

Formula (2) for the strain continues to hold when saturation has been attained in the range $\bar{\sigma} > \bar{\sigma}_s$ with l fixed at the value $d_s/2$. In this state, the fibers are fully debonded and are all carrying the axial load. There is a minor variation of the axial stress along the fibers due to the frictional 'clamping' of the matrix segments. In the fully debonded state, type I boundary conditions of HJ become applicable because there are no longer segments of undebonded material to impose the transverse constraint associated with type II conditions. The shear lag approximation to E_c, given by (3) and (7a), is essentially exact in this state, assuming that the matrix is still in contact with the fiber. Thus, for stress levels above $\bar{\sigma}_s$, overall stress and strain increments are related by $\Delta\bar{\epsilon} = \Delta\bar{\sigma}/E_c$. Type I conditions with $\nu_f = \nu_m$ give the following expression for the modulus E_c of the composite with saturated matrix cracks,

$$\frac{1}{E_c} = \frac{1}{E}\left(1 + \frac{(1-f)E_m}{fE_f\chi^2}\right). \tag{20}$$

If χ is taken to be unity (it is nearly always within a few percent of unity), the above reduces to the result $E_c = fE_f$, which would be expected were it not for the interaction of the fiber and the cracked matrix through Poisson contraction effects when the fiber remains in contact with the matrix.

Assuming fiber/matrix contact is maintained with the friction stress τ still operating, the composite strain in the fully debonded state is given by

$$\bar{\epsilon} = \frac{\bar{\sigma}}{E_c} - \frac{\sigma_f^R}{E_f} - \frac{\tau d_s}{2E_fR}. \tag{21}$$

The second term is the residual strain in the fiber, which is largely released in the saturated state. The third term is the strain resulting from

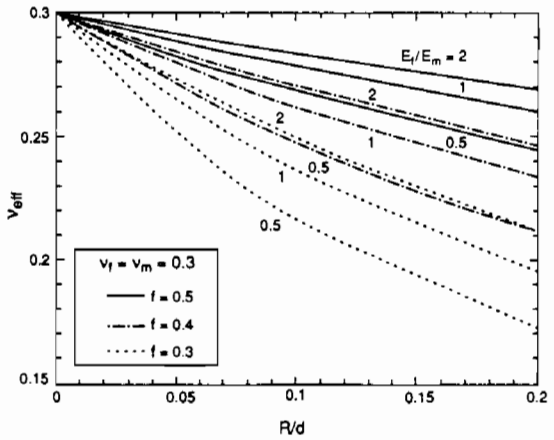

Fig. 12. Effective Poisson's ratio governing transverse strain under axial load for a composite which has undergone matrix cracking with spacing d but no debonding. The effect of initial residual stress is not included.

the friction 'clamping' stress on each segment between matrix cracks. The latter has been determined using a simple shear lag calculation which neglects any Poisson interaction between the fiber and the matrix (which *is* accounted for in the third term in (2) as it stands). This result also applies when fibers have broken, assuming this occurs beyond matrix crack saturation. Then f should be identified with the effective volume fraction of fibers, or portions of fibers, carrying their full share of the applied stress. Finally, if the fibers and the matrix have lost contact and the friction stress is lost, then (21) holds with $E_c = fE_f$ and the third term omitted.

4.5. Transverse strain

The cell model can also be used to predict the overall transverse strain $\bar{\epsilon}_T$ of the composite in the various regimes of matrix cracking. There is a substantial literature on elastic properties of uncracked composites, and no attempt will be made here to summarize results in that regime. A limited set of results obtained by the finite element analysis of the cell of Fig. 4 is displayed in Fig. 12, showing the effect of matrix crack spacing on the effective Poisson's ratio in the absence of any debonding ($l = 0$) or residual stress. In this figure, $\nu_{eff} \equiv -\bar{\epsilon}_T/\bar{\epsilon}$ and the values of the Poisson's ratios used in the calculation are $\nu_f = \nu_m = 0.3$.

With minor extension, the results of HJ can be used to give general formulas for the transverse strain in the regime in which matrix crack saturation has been achieved and the fibers are fully debonded. Neglecting the very small effect due to frictional clamping on the transverse strain, one can extend the HJ analysis to compute the change in radius ΔB of the outer boundary of the cell. This is computed with B as the value in the unloaded, uncracked state, subject to residual stresses associated with the mismatch Ω. With $\bar{\epsilon}_T$ defined as $\Delta B/B$, this analysis gives

$$\bar{\epsilon}_T = -\nu_{eff}\bar{\epsilon} + C_\Omega \Omega, \tag{22a}$$

where

$$\nu_{eff} = \frac{2f}{(1-f)} \frac{[b_1(1-fa_1)+fa_3]}{[b_2(1-fa_1)+fa_5]}, \tag{22b}$$

$$C_\Omega = \left[\nu_{eff} b_2 + \frac{f}{(1-f)}(-2b_1+\nu_m)\right] a_2. \tag{22c}$$

The coefficients in these equations are those of HJ for type I conditions. For $\nu_f = \nu_m = \nu$,

$$\nu_{eff} = \frac{2\nu f E_f}{[1+\nu+f(1-\nu)]E_f + (1-f)(1+\nu)(1-2\nu)E_m} \tag{23a}$$

and, in addition, if $E_f = E_m$, then

$$\nu_{eff} = \frac{\nu f}{[f+(1-f)(1-\nu^2)]}$$

and

$$C_\Omega = \nu_{eff}(1-f)(1+\lambda\nu), \tag{23b}$$

where λ is the ratio of the radial to axial mismatch strains defined in HJ.

The above results only apply in the range in which $\bar{\epsilon}$ exceeds $\bar{\epsilon}_s$, the strain at which the matrix cracks saturate, and is less than $\bar{\epsilon}_0$, the strain at which the fibers lose contact with the matrix. The HJ model (type I conditions apply) gives for the axial strain at which the radial compression across the fiber/matrix interface drops to zero:

$$\bar{\epsilon}_0 = [\lambda/\nu_f + (a_2 - 2\nu_f a_4)E_m/E_f]\Omega$$
$$= [\lambda/\nu + (1-f)E_m/E]\Omega, \tag{24}$$

Table 1
Constituent properties for composite systems

	SiC/CAS	SiC/SiC
E_f (GPa)	200	200
E_m (GPa)	100	300
R (μm)	7	7
ν	0.25	0.25
f	0.4	0.4
τ (MPa)	20	150
Γ_i (J m^{-2})	0.1	6
σ_m^R (MPa)	80	100
$\bar{\sigma}_{mc}$ (MPa)	125	350
$\bar{\sigma}_s$ (MPa)	275	700
$\bar{d}_s/R$	11	2

where the second expression applies when $\nu_f = \nu_m = \nu$. This estimate of the strain at which contact is lost across the fiber/matrix interface takes no account of any possible increase in effective radial mismatch due to sliding in combination with fiber surface roughness. An example showing the variation of the transverse strain as a function of the axial strain will be given at the end of the next section.

5. Stress–strain curves

To illustrate application of the results presented above we will present theoretical stress–strain curves for two unidirectional composites (Beyerle et al., 1992; Evans et al., 1993; Guillaumat, 1993), one with relatively low frictional sliding stress and interface debonding toughness (SiC/CAS) and the other with relatively large values of these properties (SiC/SiC). In each case, the fiber is nicalon SiC. The constituent properties and summarized in Table 1. In each case $\bar{\sigma}_{mc}$ and $\bar{\sigma}_s$ have been experimentally determined as, respectively, the stress at which matrix cracks first begin to spread and the stress at which matrix cracks saturate. The experimental data on the matrix crack density development indicate that the density varies approximately linearly with applied stress in the range, $\bar{\sigma}_{mc} < \bar{\sigma} < \bar{\sigma}_s$, according to Evans et al. (1993)

$$\frac{1}{d} = \frac{1}{d_s}\left(\frac{\bar{\sigma} - \bar{\sigma}_{mc}}{\bar{\sigma}_s - \bar{\sigma}_{mc}}\right). \tag{25}$$

In carrying out the calculations of the tensile stress–strain curves, we will use the saturation matrix crack spacing, d_s, from the consistency condition (16) rather than the experimentally observed average crack spacing at saturation, for reasons discussed in Section 4.2. The results for d_s, obtained from (16) for both the more accurate model and the shear lag model, are:

SiC/CAS:

$(d_s/R)_{\text{accurate model}} = 16.9$

and

$(d_s/R)_{\text{shear lag}} = 17.1,$

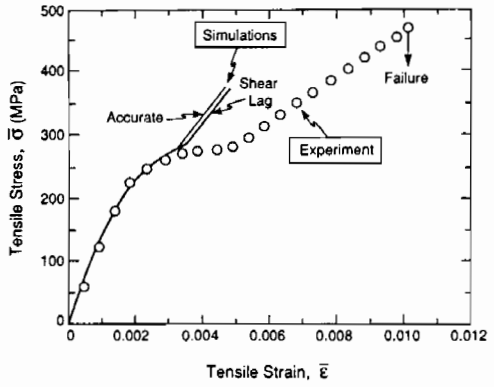

Fig. 13. Theoretical stress–strain curves for the SiC/CAS composite and comparison with experimental data.

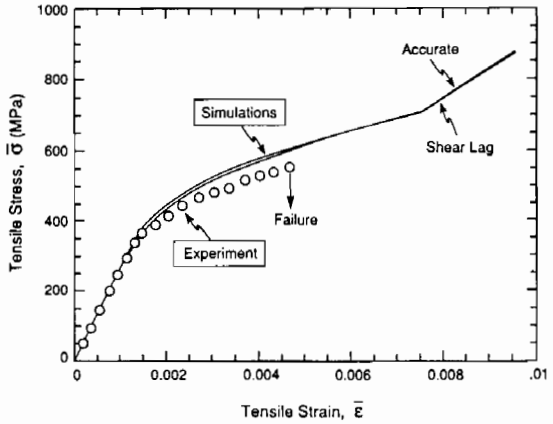

Fig. 14. Theoretical stress–strain curves for the SiC/SiC composite and comparison with experimental data.

SiC/SiC:

$$(d_s/R)_{\text{accurate model}} = 3.6$$

and

$$(d_s/R)_{\text{shear lag}} = 4.3. \quad (26)$$

These are larger than the experimentally observed average values (Table 1). There is little difference between the two theoretical values of d_s. The experimental values for the average matrix crack spacing at saturation fall in the range between d_s and $d_s/2$, consistent with statistical arguments (Curtin, 1993).

Tensile stress–strain curves calculated for the two levels of approximation are shown in Fig. 13 for the SiC/CAS material and in Fig. 14 for the SiC/SiC material. These results were generated under the assumption that contact is maintained between the fibers and the matrix over the whole range of stress shown. It is noteworthy that, in spite of the significant differences between the two approximations in some of the coefficients and in the difference in the predicted debond lengths, there is very little difference in the predicted stress–strain curves from the two approximations. (It should be borne in mind that the value of d_s in the calculations depended on the approximations; the value in (26) appropriate for the particular approximation was used.) Moreover, while the results in these figures were computed using the appropriate coefficients from HJ for the type II cell boundary conditions, the predictions obtained from the simpler shear lag formulas in (18) through (21) are essentially indistinguishable from the more elaborate shear lag results. It follows, then, that the simpler formulas for the shear lag model can be used to predict the overall tensile stress–strain curve with essentially the same accuracy as the more accurate model, as long as d_s is derived from (19), and provided that it is understood that the predicted debond length will exceed the more accurate prediction when the debond length is small.

Comparison between the simulation and the experimental results require some discussion. For the SiC/SiC composite, there appears to be a good correspondence. However, the composite fails before matrix crack saturation occurs. This is

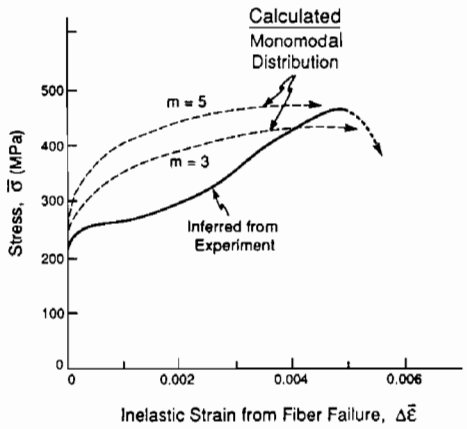

Fig. 15. Inferred inelastic strain contribution due to fiber failure for the SiC/CAS composite and comparison with the inelastic strain contribution expected from fiber failure given a monomodal distribution of fiber flaws from Hild et al. (1993). Here, m is the modulus associated with the Wibull statistics of the flaw distribution.

a consequence of the large matrix cracking stress caused by the large τ and Γ_i, as well as some fiber degradation during composite processing. For the SiC/CAS composite, there is substantial discrepancy at large strains. In this composite, the tangent modulus after matrix crack saturation is much smaller than (21) would predict (Spearing and Zok, 1993). Such a discrepancy does not arise in other composites that attain saturation prior to composite failure (Guillaumat, 1993). One implication is that the discrepancy is a consequence of fiber failure. Should this hypothesis be correct, the experimental results can be used to infer the contribution to the inelastic strain from fiber failure. The difference, $\Delta\bar{\epsilon}$, between the experimentally measured strain and the theoretical strain from Fig. 13 is plotted in Fig. 15. The shape of this curve is atypical of the inelastic strains caused by fiber failure, exemplified by simulations for a monomodal flaw distribution in the fibers (Hild et al., 1993) given by the dashed curves in Fig. 15. For fiber fialure to be responsible for the present discrepancy, it would be necessary that the fiber have a *bimodal* flaw distribution. Should this be the case, the implications for the ultimate tensile strength (UTS) need to be addressed. Preliminary analysis (Curtin, work in

progress) has indicated that the measured UTS is consistent with a bimodal distribution that indeed gives a fiber contribution to the strain compatible with Fig. 15.

There is an additional discrepancy between simulation and experiment regarding the incremental elastic modulus, E_c, measured from initial unloading data for SiC/CAS (Evans et al., 1993), as shown in Fig. 16. Under the assumption that the initial unloading response involves no reversed slipping. E_c should be given by (3) with $l = 0$, where D_1 is plotted in Fig. 7b. Specifically, for the SiC/CAS composite, the value of D_1 from Fig. 7b is ≈ 1, whereas a value ≈ 4 gives a much better fit to the experimental data. Such discrepancies are commonly found in CMCs. The phenomenon is attributed to fiber straightening effects that occur as the matrix crack density increases.

Finally, it is instructive to address the transverse strain $\bar{\epsilon}_T$ with reference to experimental data for unidirectional SiC/CAS (Harris et al., 1992) shown in Fig. 17. The model results of Section 4.5 for $\bar{\epsilon}_T$ may be cursorily compared with these data by assuming that the Poisson's ratios of the fibers and the matrix are the same, as given by the experimentally determined value for the composite, $\nu = 0.24$; the specific values of ν_f and ν_m are not known. The model results

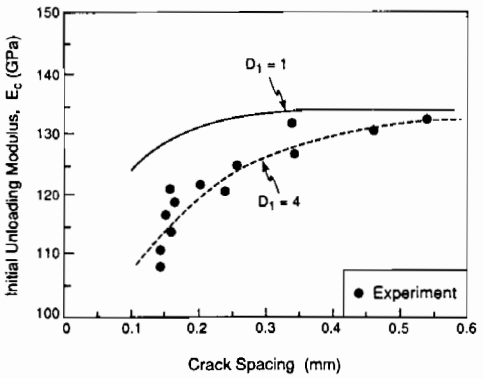

Fig. 16. Experimentally measured initial unloading modulus as a function of matrix crack spacing for the SiC/CAS uni-directional composite. Also shown are theoretical predictions from Eq. (3) for two values of D_1: the values $D_1 \approx 1$ predicted by the cell model and the value $D_1 \approx 4$ which gives a better fit to the data.

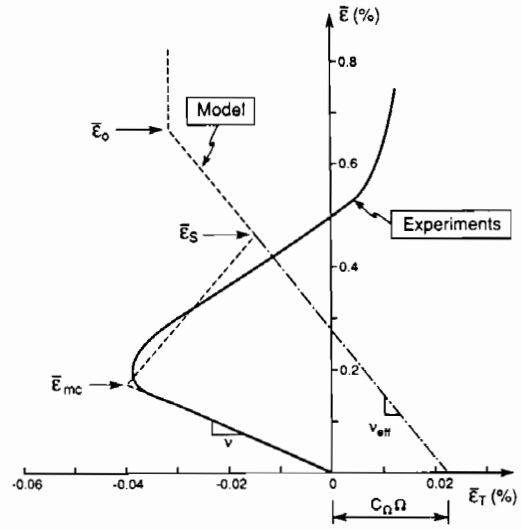

Fig. 17. Experimental data for transverse strain for SiC/CAS from Harris et al. (1992) and comparison with trends predicted by the model (Eqs. (22) and (24)).

displayed in Fig. 17 show: (i) the initial segment governed by the composite modulus ν; (ii) the segment with slope ν_{eff} from (23a) governing behavior in the regime of fully saturated matrix cracking, together with the offset $C_\Omega\ \Omega$ from (22c); (iii) a segment (arbitrarily taken to be straight) connecting (i) and (ii) between $\bar{\epsilon}_{mc}$ and $\bar{\epsilon}_s$; and (iv) the value estimated for $\bar{\epsilon}_0$ from (24), beyond which contact between fiber and matrix is lost. The model results agree quite well with the data for axial strains $\bar{\epsilon}$ less than about 0.5%, even with the simplifying assumption about the Poisson's ratios. The discrepancy with the data at larger axial strains coincides with a similar discrepancy found above for the axial inelastic strain, attributed to an influence of fiber failure. Analysis of the effects of fiber failure on $\bar{\epsilon}_T$ has yet to be performed.

6. Concluding remarks

The inelastic strain caused by matrix cracking in unidirectional CMCs has been analyzed using an accurate cell model. The formulae provided allow the straightforward prediction of these strains from the constituent properties, such as

Vagaggini, E., J.M. Domergue and A.G. Evans (1993), Relationships between the macroscopic performance of ceramic matrix composites and constituent properties, I: Theory and methodology, *J. Am. Ceram.* Soc., in press.

Weitsman, Y. and H. Zhu (1993), Multi-fracture of ceramic composites, *J. Mech. Phys. Solids 41*, 351–388.

Xia, Z.C., R.R. Carr and J.W. Hutchinson (1993), Transverse cracking in fiber-reinforced brittle matrix cross-ply laminates, *Acta Metall. Mater 41*, 2365–2376.

Appendix A

A.1. Approximation to D_3

The shear lag approximation to D_3 given by (7c) becomes increasingly accurate at large l. An approximation is first developed for small l, and then the two limits are combined as (11) to interpolate over the entire range of l. To obtain an approximation for small l, use is made of the following consequence of the reciprocal theorem for two independent loadings, τ and Σ, on the cell of Fig. 4

$$-2\pi R\int_0^l \tau V(z)\,\mathrm{d}z = \pi B^2(d/2)\Sigma\bar{\epsilon}. \qquad \text{(A1)}$$

Here, $\bar{\epsilon}$ is the overall strain due to τ, while $V(z)$ is the distribution of the relative tangential displacement of the crack faces due to an average normal traction Σ acting on the ends of the cell. The numerical results indicate that (7b) gives a reasonably accurate representation of K_{II} for the end load problem at short debond lengths, i.e. $K_{II} = c_1\Sigma(R\hat{E}/E_m)^{1/2}$. The relative tangential displacements of the faces of an interface crack near its tip are given by the plane strain relation $V(z) = (8K_{II}/\hat{E})\sqrt{(l-z)/2\pi}$, neglecting any effect of the second Dundurs parameter. Using these approximations in (A1) and noting the definition of D_3 in (2), gives

$$D_3 = \frac{32}{3}\sqrt{\frac{2}{\pi}}\,\frac{fc_1E}{\sqrt{\hat{E}E_m}}\sqrt{\frac{R}{l}}\,. \qquad \text{(A2)}$$

The form given by (11) was found to give the most accurate interpolation formula among several considered.

Table 1A
Values of $(A_1)_I/(A_1)_{II}$

E_f/E_m	$\nu = 0.2$	$\nu = 0.3$
0.5	0.99	0.98
1	1	1
2	1.03	1.01
3	1.06	1.21
10	1.19	1.77

A.2. Approximation to D_4

The approximation for K_{II} due to τ for small l simply makes use of the solution to the problem of a crack of length $2l$ along an interface between two semi-infinite plane strain blocks loaded by the shear traction τ. If, again, the second Dundurs parameter is taken to be zero, then $K_{II} = -\tau\sqrt{\pi l}$. This approximation is combined with the shear lag result (7d) as the interpolation formula (12).

A.3. Simplification of the shear lag results using type I boundary conditions

Certain predictions of the shear lag model of HJ are fairly sensitive to the type of boundary conditions for the cell, I or II. Discussion of some of the issues surrounding the influence of boundary conditions is given by Marshall (1992). Here we show that the important coefficient A_1 in (17) is not strongly dependent on the choice of boundary condition for many composites of interest. This same coefficient also appears in the widely used traction–displacement law for bridging fibers whose interface with the matrix has zero debond toughness and a frictional sliding stress τ (Marshall et al., 1985). In the present notation, this bridging law is $\delta = A_1\bar{\sigma}^2$, where δ is the total opening displacement due to fiber sliding. From (18b) it is seen that type I conditions, with $\nu_f = \nu_m$, give

$$A_1 = \frac{(1-f)^2E_m^2R}{2f^2E^2E_f\tau\chi^2}, \qquad \text{(A3)}$$

where χ is defined in (18d). (In passing, we note that the factor χ is not normally included in the

the interface sliding and debonding resistances. In some cases, the results do not fully account for the measured inelastic deformation. There are additional contributions from the fibers. For fibers having a monomodal flaw distribution, the additional inelastic strains caused by stochastic fiber failure are well known. These can be simply added to the matrix cracking strain. However, it remains to establish fiber failure contributions when more complex distributions exist. Such effects are believed to be responsible for the discrepancy between the measured stress–strain curve for SiC/CAS and the curve simulated using only the matrix cracking contribution. The strain caused by the fibers may also have a contribution from the straightening of initially curved fibers, as the matrix crack density increases upon loading. This effect is a possible cause of the smaller elastic unloading modulus measured on SiC/CAS than that predicted by the cell model.

The next important step is to extend the modeling to cross ply laminates, based on cracks extending into the 0° plies from tunnel cracks that have previously formed in the 90° plies (Fig. 1). Such analyses are in progress.

Acknowledgement

This work was sponsored by the Advanced Project Research Agency under the University Research Initiative Grant No. N00014-92-1808 with the University of California, Santa Barbara. The work of JWH was sponsored in part by this same grant (Subagreement P.O. #KK3007) and by the Division of Applied Sciences, Harvard University.

References

Aveston, J., G. Cooper and A. Kelley (1971), Single and multiple fracture, in: *Properties of Fiber Composites*, (Proc. National Physical Laboratories), IPC Science and Technology Press Ltd., Surrey, UK, 1971, pp. 15–26.

Beyerly, D., S.M. Spearing, F.W. Zok and A.G. Evans (1992), Damage and failure in unidirectional ceramic-matrix composites, *J. Am. Ceram. Soc. 75*, 2719–2725.

Brønsted, P.A., F.E. Heredia and A.G. Evans (1993), The in-plane shear properties of 2D ceramic matrix composites, *J. Am. Ceram. Soc.*, in press.

Budiansky, B. and L. Cui (1994), On the tensile strength of a fiber-reinforced ceramic composite containing a crack-like flaw, *J. Mech. Phys. Solids 42*, 1–19.

Cady, C., T.J. Mackin and A.G. Evans (1993), Stress redistribution and notch insensitivity in a ceramic matrix composite, *J. Am. Ceram. Soc.*, in press.

Curtin, W.A. (1993), Multiple matrix cracking in brittle matrix composites, *Acta Metall. Mater. 41*, 1369–1377.

Evans, A.G. (1991), The mechanical properties of reinforced ceramic, metal and intermetallic matrix composites, *Mater. Sci. Eng.* A143, 63–76.

Evans, A.G., F.W. Zok and J.B. Davis (1991), The role of interfaces in fiber-reinforced brittle matrix composites, *Compos. Sci. Technol. 42*, 3–24.

Evans, A.G., J.M. Domergue and E. Vagaggini (1993), A methodology for relating the tensile constitutive behavior of ceramic matrix composites to constituent properties, in: R. Naslain et al., eds., *High Temperature Ceramic Matrix Composites*, Woodhead, pp. 5–35.

Gao, Y-C., Y-W. Mai and B. Cotterell (1988), Fracture of fiber reinforced materials, *J. Appl. Math. and Phys. (ZAMP) 39*, 550–572.

Guillaumat, L. (1993), Ph.D. Thesis, Laboratoire des Composites Thermostructuraux, Domaine Universitaire, Bordeaux, France.

Harris, B., F.A. Habib and R.G. Cooke (1992), Matrix cracking and the mechanical behavior of SiC-CAS composites, *Proc. R. Soc. London A437*, 109–131.

Hild, F, J.M. Domergue, F.A. Leckie and A.G. Evans (1993), Tensile and flexural ultimate strength of fiber-reinforced ceramic-matrix composites, *Int. J. Solids Struct.*, in press.

Hutchinson, J.W. and H.M. Jensen (1990), Models of fiber debonding and pullout in brittle composites with friction, *Mech. Mater. 9*, 139–163.

Kim, R.Y. and N.J. Pagano (1991), Crack initiation in unidirectional brittle-matrix composites, *J. Am. Ceram. Soc. 74*, 1082–1090.

Marshall, D.B., B.N. Cox and A.G. Evans (1985), The mechanics of matrix cracking in brittle-matrix fiber composites, *Acta. Metall. 33*, 2013–2021.

Marshall, D.B. and A.G. Evans (1985), Failure mechanisms in ceramic fiber/ceramic matrix composites, *J. Am. Ceram. Soc. 68*, 225–231.

Marshall, D.B. (1992), Analysis of fiber debonding and sliding experiments in brittle matrix composites, *Acta Metall. Mater. 40*, 427–441.

Nardonne, V.C. and K.M. Prewo (1988), Tensile performance of carbon-fiber-reinforced glass, *J. Mater. Sci. 23*, 168–180.

Pryce, A.W. and P. Smith (1992), Modelling the stress/strain behavior of unidirectional ceramic matrix composite laminates, *J. Mater. Sci. 27*, 2695–2704.

Spearing, S.M. and F.W. Zok (1993), Stochastic aspects of matrix cracking in brittle matrix composites, *J. Eng. Mater. Technol. 115*, 314–318.

bridging law. It is associated with a Poisson's ratio interaction between the fiber and matrix which is not taken into account in the simpler shear lag analyses which have been used to arrive at the bridging law coefficient.) Table A1 presents the ratio of A_1 for type I boundary conditions from (A3) to that for type II conditions computed using results from HJ for various combinations of fiber to matrix moduli and two values of Poisson's ratio. Except for large fiber to matrix moduli mismatches, the difference between the predictions for these two conditions is small.